Geophysical Research Letters

RESEARCH LETTER
10.1029/2019GL083633

Key Points:
- Density of deep mantle melts is obtained from first-principles computations
- Water effect on density of Fe-bearing hydrous melt is determined
- Hydrous melts can be negatively buoyant at lowermost mantle conditions

Supporting Information:
- Supporting Information S1

Correspondence to:
Z. Du,
duzhixue@gig.ac.cn

Citation:
Du, Z., Deng, J., Miyazaki, Y., Mao, H.-k., Karki, B. B., & Lee, K. K. M. (2019). Fate of hydrous Fe-rich silicate melt in Earth's deep mantle. *Geophysical Research Letters*, *46*, 9466–9473. https://doi.org/10.1029/2019GL083633

Received 14 MAY 2019
Accepted 29 JUL 2019
Accepted article online 1 AUG 2019
Published online 19 AUG 2019
Corrected 9 SEP 2019

This article was corrected on 9 SEP 2019. See the end of the full text for details.

Fate of Hydrous Fe-Rich Silicate Melt in Earth's Deep Mantle

Zhixue Du[1,2], Jie Deng[3], Yoshinori Miyazaki[3], Ho-kwang Mao[2,4], Bijaya B. Karki[5,6,7], and Kanani K. M. Lee[3]

[1]State Key Laboratory of Isotope Geochemistry, Guangzhou Institute of Geochemistry, Chinese Academy of Sciences, Guangzhou, China, [2]Geophysical Laboratory, Carnegie Institution of Washington, Washington, DC, USA, [3]Department of Geology and Geophysics, Yale University, New Haven, CT, USA, [4]Center for High Pressure Science and Technology Advanced Research, Shanghai, China, [5]Department of Geology and Geophysics, Louisiana State University and A&M College, Baton Rouge, LA, USA, [6]School of Electrical Engineering and Computer Science, Louisiana State University and A&M College, Baton Rouge, LA, USA, [7]Center for Computation and Technology, Louisiana State University and A&M College, Baton Rouge, LA, USA

Abstract Density of silicate melt dictates melt migration and establishes the gross structure of Earth's interior. However, due to technical challenges, the melt density of relevant compositions is poorly known at deep mantle conditions. Particularly, water may be dissolved in such melts in large amounts and can potentially affect their density at extreme pressure and temperature conditions. Here we perform first-principles molecular dynamics simulations to evaluate the density of Fe-rich, eutectic-like silicate melt (*E* melt) with varying water content up to about 12 wt %. Our results show that water mixes nearly ideally with the nonvolatile component in silicate melt and can decrease the melt density significantly. They also suggest that hydrous melts can be gravitationally stable in the lowermost mantle given its likely high iron content, providing a mechanism to explain seismically slow and dense layers near the core-mantle boundary.

Plain Language Summary Planetary-scale melting is ubiquitous after energetic impacts early in Earth's history. Therefore, determining key melt properties, such as density, is of great significance to better understand Earth's formation and subsequent evolution. In this study, we performed state-of-art first-principles molecular dynamics simulations to examine the density of deep mantle melts, namely, hydrous Fe-rich silicate melts. We find that such hydrous melts can be gravitationally stable near Earth's core-mantle boundary given their likely high iron content. This has great implications for Earth's thermochemical evolution, as well as Earth's volatile cycle.

1. Introduction

Magma oceans are thought to prevail during Earth's accretion after large impacts (e.g., Tonks & Melosh, 1993). The physical properties of relevant silicate melts are key to our understanding of how magma oceans formed and crystallized. The relative density of these melts with respect to solid minerals must have determined the direction and rate of melt migration during magma cooling thereby controlling Earth's thermochemical evolution (e.g., Labrosse et al., 2007). Melt density, however, is a complex function of temperature, pressure, and composition. Water, in particular, strongly influences melt properties and plays a crucial role in the melting process. First, during crystallization (or partial melting), water is strongly partitioned into the melt compared to the coexisting solid (e.g., Hauri et al., 2006). Therefore, trace amount of water can greatly depress the melting point and trigger deep mantle melting (e.g., Hirschmann, 2006). Second, water is likely enriched as much as ~1–10 wt % in silicate melt, greatly reducing melt density, viscosity, and enhancing electrical conductivity (e.g., Mookherjee et al., 2008). Lastly, such hydrous silicate melt, once formed, likely dominates the overall water budget in the Earth's deep mantle, becoming a significant reservoir for water. Consequently, its migration at depths can fundamentally influence Earth's deep water cycle.

Despite much effort made in recent years in investigating the behavior and physical properties of silicate melts at high pressure (e.g., Kono & Sanloup, 2018), the melt density is poorly constrained at deep mantle conditions for relevant compositions. Deep mantle melts are likely to be ultramafic and enriched in water

and iron due to their high incompatibility (e.g., Bercovici & Karato, 2003; Nomura et al., 2011). Performing experiments to measure the density of such melts is challenging. A few extant studies using static compression are limited to upper mantle conditions (e.g., Matsukage et al., 2005). While experiments using diamond anvil cells can reach up to Earth's core mantle boundary (CMB) pressure, only $MgSiO_3$ glass (an analog of $MgSiO_3$ melt) has been measured at ambient temperature (Petitgirard et al., 2015). Dynamic (shock-wave) experiments can directly determine the equation of state of silicate melts at simultaneous high pressure-high temperature conditions, but these measurements have so far focused on water-free systems, such as molten $MgSiO_3$ (Akins, 2004; Mosenfelder et al., 2009), Mg_2SiO_4 (Mosenfelder et al., 2007), and Fe_2SiO_4 (Thomas et al., 2012).

On the other hand, first-principles computational approach has an advantage of studying hydrous melts at the extreme conditions of deep mantle relevance. Previous computations have examined hydrous, Fe-free melts, such as $MgSiO_3$ (Mookherjee et al., 2008), SiO_2 (Karki & Stixrude, 2010), and model basalt (Bajgain et al., 2015). Recently, anhydrous Fe-bearing melts have been simulated to constrain the effects of Fe (Bajgain et al., 2015; Caracas et al., 2019), also considering the spin and oxidation states of iron (Karki et al., 2018). While these computations have shown that water can significantly affect the melt density, a direct evaluation of water effects on the density of Fe-rich silicate melts is still lacking.

The goal of this study is to examine the effects of water on the density of Fe-rich ultramafic melts and obtain a universal equation of state for deep mantle melts of relevant compositions. We also discuss geophysical implications for melting processes in Earth's deep mantle.

2. Methods

First-principles molecular dynamics (FPMD) simulations were performed in *NVT*-canonical ensemble using the projector augmented wave potentials and generalized gradient approximation as implemented in the VASP software (Kresse & Furthmüller, 1996). We take an eutectic-like melt to represent a composition of relevance to deep mantle ($Mg/Si = 1$, $Fe^{\#} = Fe/(Fe + Mg) = 0.47$ with various water contents, referred to as *E* melt hereafter; e.g., Boukaré et al., 2015; Ohnishi et al., 2017). The supercells consist of $x MgSiO_3 \bullet y FeO \bullet z H_2O$ with five different sets of *x*, *y*, *z* as compiled in Table S1. The volume of the supercell was varied between 906.5 and 1,379.8 $Å^3$ to generate a wide range of pressure (6.7 to 153.8 GPa) at 4,000 K. The iron was set in low-spin (nonmagnetic) state for all simulations to isolate the effects of water on melt density. The plane wave cutoff was set at 400 eV with Gamma point Brillouin zone sampling, which resulted in the Pulay stress of 4 to 9 GPa over the volume range considered. The simulations were run for 5 to 10 picoseconds with time step of 1 femtosecond. Pure water was also simulated as a function of pressure at 4,000 K using the $H_{48}O_{24}$ supercell. Further details about the first-principle molecular dynamics simulations of silicate melts can be found elsewhere (e.g., Karki et al., 2018).

3. Results and Discussion

3.1. Speciation of Water in the Eutectic-Like Melt

We take a eutectic-like melt of $16 MgSiO_3 \bullet 14 FeO \bullet 20 H_2O$ (E13–16) as an example to study the evolution of water speciation with pressure. The general trend is that hydrogen and oxygen become increasingly polymerized with pressure, consistent with previous computational studies (Figure S1; Bajgain et al., 2015; Karki & Stixrude, 2010). The H-O coordination environment consists of different species, including uncoordinated, one-fold, two-fold and three-fold coordination, whose proportions change with pressure (Figure 1a). At pressures below 50 GPa, the dominant H-O coordination is onefold, corresponding to hydroxyls (Figure 1a). Two-fold coordination prevails at higher pressures, corresponding to polyhedral H bridging and extended forms (Figure 1a). It is remarkable that the mean H-O coordination of hydrous melt is almost identical with that of the pure water over the entire pressure range considered (Figure 1b).

3.2. Partial Molar Volume of Water

Partial molar volume (V_m) of water in the melt can be calculated using $V_m = (V - V_0)/n$, where V is the volume of hydrous melt, V_0 is the volume of anhydrous melt, and n is the number of water "molecules" in the supercell. The V_m results at 4,000 K shown in Figure 2 are comparable with the previous

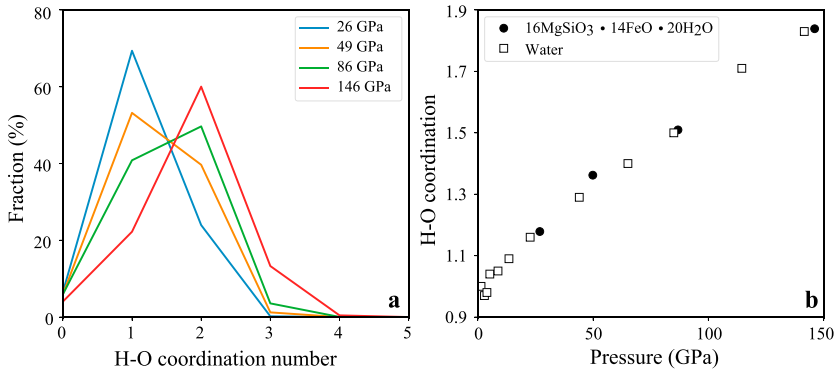

Figure 1. Evolution of water speciation of eutectic-like silicate melt (*E* melt) and pure water. (a) Proportions of various H-O coordination species. (b) Mean H-O coordination numbers of *E* melt and pure water.

calculations on hydrous basaltic melt (Bajgain et al., 2015). The partial molar volume of water thus appears to be weakly sensitive to melt composition over a wide pressure regime. We also present the equation of state of pure water (V_{pw}) from 0 to 150 GPa at 4,000 K in Figure 2 (with the fit parameters listed in Table S2) and find that the partial molar volume of water in melt is almost equal to the pure water volume at all pressures. This suggests ideal mixing behavior between water and the nonvolatile components in silicate melt over the pressure regime 27 to 150 GPa investigated in this study. As previously shown for Fe-free basaltic melt (Bajgain et al., 2015), this ideal mixing behavior extends to much lower pressures (Figure 2). It is interesting to explore whether this holds in the presence of Fe. Nonetheless, we focus on the implications at CMB pressure ~135 GPa, where ideal-mixing behavior of water is expected to occur in both Fe-rich and Fe-free melts (Figure 2).

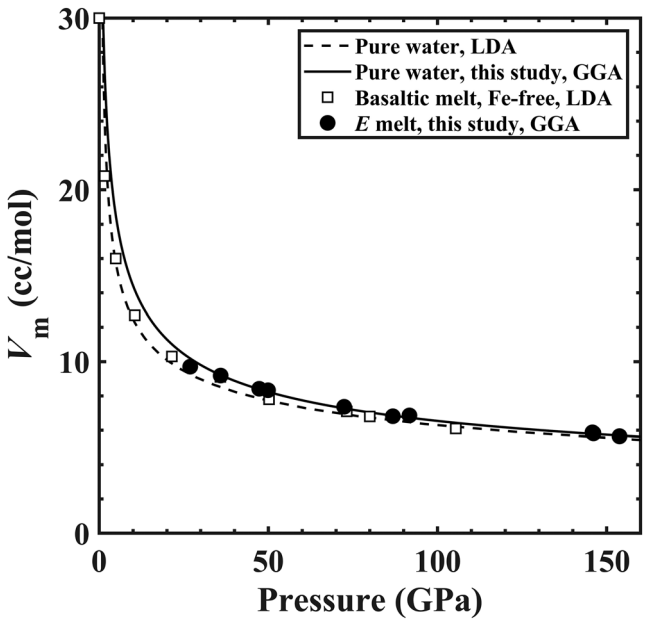

Figure 2. Calculated partial molar volume (V_m) of water in eutectic-like silicate melt (*E* melt) at 4,000 K at high pressure. Filled circles are our results for *E* melt, compared with previous computational results (open squares) for Fe-free model basalt melt (Bajgain et al., 2015). Solid and dashed curves are the equations of state for pure water at 4,000 K, with general gradient approximation (GGA; this study) and local density approximation (LDA; Bajgain et al., 2015), respectively.

3.3. Densities of Hydrous Silicate Melt

The simulation results are given in Table S1 for *E* melts with different water contents (3.98, 9.43, and 12.13 wt %) in the pressure range 27–153 GPa at 4,000 K. The pressure-volume relationship for anhydrous *E* melt (E01–06) at 4,000 K can be described with a fourth-order Birch Murnaghan equation of state: $V_0 = 2{,}480 \pm 91$ Å^3, $K_0 = 20.29 \pm 6$ GPa, $K' = 4.62 \pm 0.69$, and $K'' = -0.19 \pm 0.17$ GPa^{-1}, with uncertainties that are 1σ errors (Table S2). As shown in Figure 3a, the density profiles of hydrous *E* melts are systematically shifted downward from the anhydrous melt density as water lowers the melt density considerably. We can also evaluate the density of anhydrous *E* melt by combining the results for bridgmanite and ferropericlase liquids as done by Karki et al. (2018). Thus derived density profile almost matches with the one directly obtained in this study (Figure 3a).

As shown earlier, water is mixed ideally with nonvolatile components in silicate melt, particularly at high pressures (>25 GPa). Therefore, the density of hydrous silicate melt (ρ) can be calculated as follows:

$$\rho = (1-x)\rho_0 + x\,\rho_w \quad (1)$$

where ρ_0 is the melt density of nonvolatile component, ρ_w is the density of pure water, and x is the volume fraction of water.

From equation (1), we can also define density contrast: $\frac{\rho}{\rho_0} - 1 = \left(1 - \frac{\rho_w}{\rho_0}\right)x \sim \alpha X_{H_2O}$, when ρ_w/ρ_0 approaches to a constant at high pressure. Therefore, the effects of water can be approximated as linearly dependent on water content (X_{H_2O} in wt %) with coefficient α. We apply a weighted linear

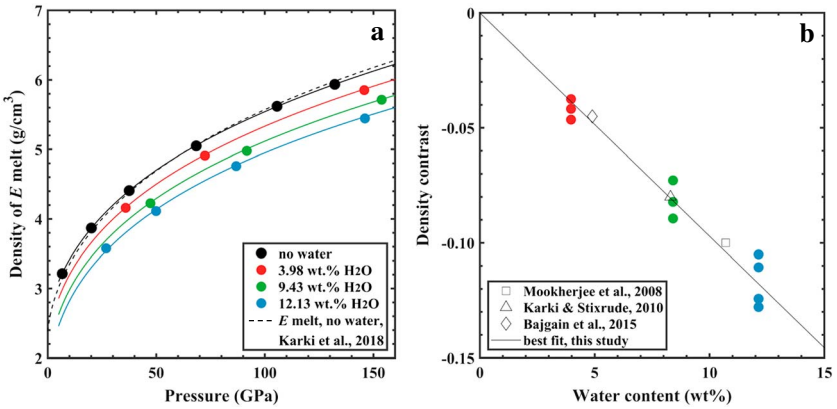

Figure 3. (a) Density-pressure profiles of anhydrous and hydrous eutectic-like silicate melt (*E* melt) at 4,000 K. The calculated results are shown by black circles (no water), and by red, green, and blue circles, respectively, for 3.98, 9.43, and 12.13 wt % water content. The solid curves represent the density profiles from the EoS fit and the ideal water-melt solution model (equation (1)). The dashed curve is the density derived from Karki et al. (2018). (b) Density contrast between hydrous and anhydrous *E* melts as a function of the water content at 4,000 K. The present results for *E* melt (solid circles) show a linear trend (solid line). Also shown are the previous results for molten silica (Karki & Stixrude, 2010), enstatite (Mookherjee et al., 2008), and model basalt (Bajgain et al., 2015).

regression to the calculated melt densities of *E* melts and obtain $\alpha = -0.97 \pm 0.02$ with $R^2 = 0.98$ (Figure 3b). We also examine the results for other hydrous silicate melts (though not included them in the regression). It is remarkable that the hydrous effects on melt density for $MgSiO_3$ (Mookherjee et al., 2008), model basalt (Bajgain et al., 2015), and silica (Karki & Stixrude, 2010) follow our predicted linear trend with water content. This is likely due to the speciation of water in silicate melt at high pressures (Figures 1 and 2). The linear approximation, however, is less accurate at high water content, which results in more scatter (Figure 3b).

4. Implications

The longevity of partial melt at the CMB is mostly governed by its relative density, which, in turn, is controlled by melt composition, particularly, Fe and water contents (e.g., Labrosse et al., 2007; Stevenson, 2008). Here, we first briefly review current knowledge about partitioning of Fe and water between a solid and silicate melt. Exchange reaction of Fe between a solid and silicate melt can be described as follows:

$$FeO^{melt} + MgO^{solid} \rightleftharpoons MgO^{melt} + FeO^{solid}$$

with the exchange coefficient defined as $K_{Fe} = \frac{Fe_s^{\#}\left(1-Fe_L^{\#}\right)}{Fe_L^{\#}\left(1-Fe_s^{\#}\right)}$, where $Fe_L^{\#}$ and $Fe_s^{\#}$ represent the iron contents (defined as molar ratio Fe/(Fe + Mg)) of silicate melt and coexisting solid, respectively. The measured values of K_{Fe} for bridgmanite range from 0.3–0.4 at 25 GPa (Corgne et al., 2005) to ~0.1 at 80–140 GPa (Nomura et al., 2011; Tateno et al., 2014). For ferropericlase (Mg,Fe)O, K_{Fe} is ~0.1–0.3 at 3–80 GPa (Deng & Lee, 2017; Du & Lee, 2014) to ~0.1 up to 120 GPa (Fu et al., 2018). K_{Fe} might also depend on the temperature, bulk composition, and water content, and future studies should explore those effects. Here we take 0.1–0.2 as relevant K_{Fe} range for the CMB.

No data on partitioning of water (D_{H2O}) between silicate melt and lower mantle minerals are currently available. Here we estimate D_{H2O} using the relation: $D_{H2O} = C_{mineral}/C_{melt}$, where C_{melt} and $C_{mineral}$ are the water solubilities in silicate melt and mineral, respectively. The solubility of water in mantle melts is expected to be high (>50 wt %) at pressures greater than 4 GPa, beyond which miscibility gap between hydrous fluid and silicate melt closes and it becomes a supercritical fluid (e.g., Mibe et al., 2007). However, the data on the water solubility in lower mantle minerals are highly scattered. The measured water solubility of bridgmanite is as low as ~1–2 ppm (Bolfan-Casanova et al., 2000) but also takes higher values of ~200 ppm (Meade et al., 1994) and up to 2,000 ppm in Al- and Fe-bearing bridgmanite (Inoue et al., 2010; Litasov et al., 2003; Murakami et al., 2002). Computational studies have predicted the

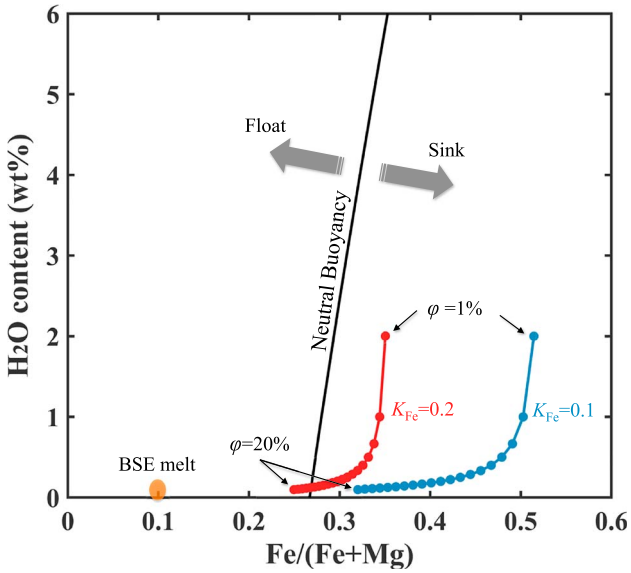

Figure 4. Density difference between silicate melt and solid mantle at the CMB condition (4,000 K and 135 GPa) in composition space defined by water and iron contents. Contour of zero density difference (neutral buoyancy) considering melt with (Mg + Fe)/Si = 2 is drawn as a black line. The thick arrows labeled as "Float" and "Sink" indicate the areas where density differences are negative and positive, respectively. Melt with bulk silicate Earth (BSE melt) composition (Mg/Si = 1.25, $Fe^{\#}$ = 0.1, with no water) is shown as an orange circle. Density of the melt is calculated assuming equilibrium crystallization as melt fraction φ ranges from 20 to 1% at the step of 1% for K_{Fe} = 0.2 and 0.1. K_{Fe} represents the exchange coefficient of Fe in exchange reaction between a solid and silicate melt.

water solubility in bridgmanite in the range ~33 ppm (Panero et al., 2015) to 1,000 ppm (Hernández et al., 2013). In addition, the water solubility of another major lower mantle mineral MgO tends to be rather low too, ~20 ppm at 25 GPa and 1,200 °C (N. Bolfan-Casanova et al., 2002). In this study, we take 1–1,000 ppm as a possible range for the solubility of water in bridgmanite, which corresponds to D_{H2O} ~2×10^{-6}–2×10^{-3}.

Given that both K_{Fe} and D_{H2O} values are much smaller than 1, melt should be much more enriched in both Fe and water than the solid at equilibrium. To demonstrate the importance of compositional effects, we use equation (1) to compute the melt density as a function of water content and Fe content ($Fe^{\#}$) at the CMB condition, namely, 135 GPa and 4,000 K. We also use the density model from Karki et al. (2018) to calculate ρ_0 for different Fe contents with the low- to high-spin Fe ratio set at 80:20. Figure 4 shows a contour of density difference equal to zero between a silicate melt and solid (i.e., neutral density buoyancy) at the CMB condition. For simplicity, (Mg + Fe)/Si of the melt is taken as 2 (Boukaré et al., 2015; Ohnishi et al., 2017) as densities of MgO and $MgSiO_3$ melt are similar at high pressure (Karki et al., 2018). The solid density of Earth's lowermost mantle is taken as 5.566 g/cm^3 (Dziewonski & Anderson, 1981). Both water content and $Fe^{\#}$ have strong effects on the melt density, thereby splitting the composition space into two areas, each on either side of the black line (Figure 4) indicated by "Float" and "Sink" arrows. The melt will float, for example, when the density difference is negative for low iron-high water content, and the melt will sink, for example, when the density difference is positive for high iron-low water contents.

To determine the fate of the melt, we need to find the exact water and iron contents in the partial melt. However, this is uncertain due to a few but poorly constrained parameters, such as the melt fraction (φ), exchange coefficient of iron (K_{Fe}), and partition coefficient of water (D_{H2O}) between melt and coexisting solids, as well as bulk iron and water contents (X_{Fe} and X_{H2O}).

Following Karki et al. (2018), we consider a scenario for crystallization of a fully molten Earth, assuming equilibrium crystallization (Solomatov & Stevenson, 1993b). We further assume initial uniform iron and water contents in the magma ocean as $X_{Fe} = 0.1$ and $X_{H2O} = 200$ ppm, respectively. We estimate water content of the silicate melt using $X_{melt,H_2O} = \frac{X_{H_2O}}{(1-\varphi)D_{H_2O}+\varphi}$. In our case, D_{H2O} ~2×10^{-6}–2×10^{-3}, which implies $(1-\varphi)D_{H_2O} \ll \varphi$. Therefore, $X_{melt,H_2O} \sim X_{H2O}/\varphi$, which means that water content in silicate melt is a strong function of initial water content and melt fraction.

We calculate the density differences between the melt and solid mantle for different amounts of partial melts by varying φ from 20% to 1%. The calculated $Fe^{\#}$ in the melt ranges ~0.25–0.50 and water content ranges ~500 ppm–2 wt %. In this case (K_{Fe} = 0.1), equilibrium compositional evolution (blue curve) falls in the region where melt is denser than coexisting solid. Therefore, residual melt may migrate downward and stay negatively buoyant above the CMB. For K_{Fe} = 0.2, at early stage of crystallization when $\varphi > 15\%$, the melt is more buoyant than coexisting solid; therefore, crystallization should start from bottom-up and melt would migrate upward. Toward later stage when $\varphi < 15\%$, the residual melt is denser than coexisting solid and would migrate downward. We find that the upper and lower bounds of D_{H2O} yield very similar evolution curves; therefore, only one curve is shown in Figure 4. In both cases, almost all water would go to the silicate melt and the calculated water contents are similar at given melt fraction φ (note that two evolution curves run almost parallel in the vertical direction).

We note that water contents are below 0.2 wt % in the melt during early stage of crystallization of magma ocean when melt fraction $\varphi > 10\%$ (Figure 4). So the density crossover is essentially dominated by Fe enrichment in the melt. These evolution scenarios are similar to the previous studies for a water-free

magma ocean (e.g., Caracas et al., 2019; Karki et al., 2018; Miyazaki & Korenaga, 2019) when $\varphi > 10\%$. During such early stages of crystallization, the details of how crystal settled are still debated and model dependent (e.g., Abe, 1997; Solomatov & Stevenson, 1993a). Nonetheless, it is conceivable to form a BMO either by matrix compaction and/or by late overturn (Elkins-Tanton et al., 2003; Miyazaki & Korenaga, 2019). In this study, we focus on the evolution of a basal magma ocean near the CMB at late stage of crystallization ($\varphi < 10\%$), when water gets increasingly enriched in the residual melt. As shown in Figure 4, when $\varphi < 10\%$, the residual melt can contain a few weight percent water and be gravitationally stable near the CMB.

We assume a constant temperature of 4,000 K at the CMB. This is not likely the case, considering that the Earth is cooling down (e.g., Korenaga, 2008). In our case, high water content in the melt likely decreases the crystallization temperature (Nomura et al., 2014) and a lower CMB temperature might be expected. The density differences between melt and coexisting solid are expected to be more or less insensitive to temperature directly at high pressures because the thermal expansivity is small for both the solid and liquid phases ($1–2 \times 10^{-5}$ K^{-1}; Karki et al., 2018). Moreover, temperature might influence Fe or water partitioning between solid and liquid, affecting the density difference between the two. Therefore, temperature effects should be taken into account in future studies, especially its effect on Fe/water partitioning between solid and liquid.

In addition, we test the sensitivity of our model parameters, with a range of X_{Fe} and X_{H2O}. We find that corresponding evolution curves are similar (Figures S2 and S3). Fractional crystallization may also be considered as crystal accumulation and matrix compaction are likely important (Miyazaki & Korenaga, 2019). If so, it should result in higher Fe content in the melt at a given melt fraction, further stabilizing silicate melt at CMB.

The hydrous, iron-rich melt is also expected to be low in seismic velocities (e.g., Williams & Garnero, 1996). This is corroborated with seismological observations suggesting the existence of ultralow-velocity zones near the CMB (e.g., Williams & Garnero, 1996; Yuan & Romanowicz, 2017). Other geophysical observations, such as normal modes and tidal tomography, also indicate a dense layer in the lowermost mantle (e.g., Ishii & Tromp, 1999; Lau et al., 2017; Trampert et al., 2004), consistent with such a dense, hydrous iron-rich melt layer.

Similar to water, heat-producing elements (e.g., potassium, uranium and thorium) are regarded as highly incompatible, although their partitioning behavior at CMB conditions is yet to be determined (e.g., Corgne et al., 2005; Hirose et al., 2004). If they remain incompatible at CMB condition, hydrous melts can also be a significant heat source throughout Earth's history (Labrosse et al., 2007). This can have profound implications for Earth's heat budget and its thermal history (e.g., Driscoll & Bercovici, 2014; Korenaga, 2008). Moreover, noble gases (e.g., helium) are also considered to have strong affinity for silicate melts; thus, a primordial layer with high $^3He/^4He$ ratios may have formed early and remained near the CMB and isolated from the overlying convecting mantle (e.g., Kurz et al., 1982).

5. Conclusions and Future Studies

We perform first-principles molecular dynamics simulations of hydrous iron-rich silicate melts at 4,000 K in the pressure range between 27–153 GPa. Various water contents are chosen to systematically determine the effects of water on the density of silicate melt. We find that water decreases melt density significantly and mixes nearly ideally with nonvolatile components in silicate melts over the pressure range studied. By evaluating melt-solid density differences over a wide composition space defined by iron and water contents, we infer that hydrous partial melts can be denser than coexisting solids at the later stages of magma ocean crystallization when melt fractions are less than ~15%. Therefore, hydrous melt can be gravitationally stable under CMB conditions for geological time scales. This might provide a mechanism to explain seismically slow and dense layers near the CMB. Our study also highlights the importance of precisely determining solid-liquid partitioning coefficients of iron and water at deep mantle conditions. Improved data will help constrain the $Fe^{\#}$ and water content in partial melts, thus providing a better understanding of the stability of partial melts at the CMB. Effects of other volatiles, such as carbon, should be also included in the future to evaluate the stability of partial melt at the CMB (e.g., Ghosh et al., 2017; Solomatova et al., 2019).

Understanding the fate of these volatile-rich melts will be the key to unfolding Earth's early history and thermochemical evolution.

Acknowledgments
This work is supported by grants from Chinese Academy of Sciences and State Key Laboratory of Isotope Geochemistry (29Y93301701, 51Y8340107 to Z. Du) and from NSF (EAR-1321956, EAR-1551348 to K.K.M. Lee and EAR-1764140 to B.B. Karki). This is contribution No.IS-2732 from GIGCAS. We benefited greatly from discussions with Shun Karato, Peng Ni, Yuan Li, Colin Jackson and Peter Driscoll. We also appreciate comments from two anonymous reviewers. We thank the Yale Center for Research Computing and Louisiana State University High Performance Computing for computing support and resources. All data presented in this paper are in Table S1. Parameters of the input files are described in section 2.

References

Abe, Y. (1997). Thermal and chemical evolution of the terrestrial magma ocean. *Physics of the Earth and Planetary Interiors*, *100*(1-4), 27–39. https://doi.org/10.1016/S0031-9201(96)03229-3

Akins, J. A., Luo, S.-N., Asimow, P. D., & Ahrens, T. J. (2004). Shock-induced melting of $MgSiO_3$perovskite and implications for melts in Earth's lowermost mantle. *Geophysical Research Letters*, *31*, L14612. https://doi.org/10.1029/2004GL020237

Bajgain, S., Ghosh, D. B., & Karki, B. B. (2015). Structure and density of basaltic melts at mantle conditions from first-principles simulations. *Nature Communications*, *6*(1), 8578. https://doi.org/10.1038/ncomms9578

Bercovici, D., & Karato, S. (2003). Whole-mantle convection and the transition-zone water filter. *Nature*, *425*(6953), 39–44. https://doi.org/10.1038/nature01918

Bolfan-Casanova, N., Keppler, H., & Rubie, D. C. (2000). Water partitioning between nominally anhydrous minerals in the $MgO–SiO_2–H_2O$ system up to 24 GPa: Implications for the distribution of water in the Earth's mantle. *Earth and Planetary Science Letters*, *182*(3-4), 209–221. https://doi.org/10.1016/S0012-821X(00)00244-2

Bolfan-Casanova, N., Mackwell, S., Keppler, H., McCammon, C., & Rubie, D. C. (2002). Pressure dependence of H solubility in magnesiowustite up to 25 GPa: Implications for the storage of water in the Earth's lower mantle. *Geophysical Research Letters*, *29*(10), 89-1. https://doi.org/10.1029/2001gl014457

Boukaré, C. E., Ricard, Y., & Fiquet, G. (2015). Thermodynamics of the MgO-FeO-SiO_2 system up to 140 GPa: Application to the crystallization of Earth's magma ocean. *Journal of Geophysical Research: Solid Earth*, *120*, 6085–6101. https://doi.org/10.1002/2015JB011929

Caracas, R., Hirose, K., Nomura, R., & Ballmer, M. D. (2019). Melt–crystal density crossover in a deep magma ocean. *Earth and Planetary Science Letters*, *516*, 202–211. https://doi.org/10.1016/j.epsl.2019.03.031

Corgne, A., Liebske, C., Wood, B. J., Rubie, D. C., & Frost, D. J. (2005). Silicate perovskite-melt partitioning of trace elements and geochemical signature of a deep perovskitic reservoir. *Geochimica et Cosmochimica Acta*, *69*(2), 485–496. https://doi.org/10.1016/j.gca.2004.06.041

Deng, J., & Lee, K. K. M. (2017). Viscosity jump in the lower mantle inferred from melting curves of ferropericlase. *Nature Communications*, *8*(1), 1997. https://doi.org/10.1038/s41467-017-02263-z

Driscoll, P., & Bercovici, D. (2014). On the thermal and magnetic histories of Earth and Venus: Influences of melting, radioactivity, and conductivity. *Physics of the Earth and Planetary Interiors*, *236*, 36–51. https://doi.org/10.1016/j.pepi.2014.08.004

Du, Z., & Lee, K. K. M. (2014). High-pressure melting of MgO from (Mg,Fe)O solid solutions. *Geophysical Research Letters*, *41*, 8061–8066. https://doi.org/10.1002/2014GL061954

Dziewonski, A. M., & Anderson, D. L. (1981). Preliminary reference Earth model. *Physics of the Earth and Planetary Interiors*, *25*(4), 297–356. https://doi.org/10.1016/0031-9201(81)90046-7

Elkins-Tanton, L. T., Parmentier, E. M., & Hess, P. C. (2003). Magma ocean fractional crystallization and cumulate overturn in terrestrial planets: Implications for Mars. *Meteoritics & Planetary Science*, *38*(12), 1753–1771. https://doi.org/10.1111/j.1945-5100.2003.tb00013.x

Fu, S., Yang, J., Zhang, Y., Liu, J., Greenberg, E., Prakapenka, V. B., et al. (2018). Melting behavior of the lower-mantle ferropericlase across the spin crossover: Implication for the ultra-low velocity zones at the lowermost mantle. *Earth and Planetary Science Letters*, *503*, 1–9. https://doi.org/10.1016/j.epsl.2018.09.014

Ghosh, D. B., Bajgain, S. K., Mookherjee, M., & Karki, B. B. (2017). Carbon-bearing silicate melt at deep mantle conditions. *Scientific Reports*, *7*(1), 848. https://doi.org/10.1038/s41598-017-00918-x

Hauri, E., Gaetani, G., & Green, T. (2006). Partitioning of water during melting of the Earth's upper mantle at H_2O-undersaturated conditions. *Earth and Planetary Science Letters*, *248*(3-4), 715–734. https://doi.org/10.1016/j.epsl.2006.06.014

Hernández, E. R., Alfè, D., & Brodholt, J. (2013). The incorporation of water into lower-mantle perovskites: A first-principles study. *Earth and Planetary Science Letters*, *364*, 37–43. https://doi.org/10.1016/j.epsl.2013.01.005

Hirose, K., Shimizu, N., van Westrenen, W., & Fei, Y. (2004). Trace element partitioning in Earth's lower mantle and implications for geochemical consequences of partial melting at the core–mantle boundary. *Physics of the Earth and Planetary Interiors*, *146*(1-2), 249–260. https://doi.org/10.1016/j.pepi.2002.11.001

Hirschmann, M. M. (2006). Water, melting, and the deep Earth H_2O cycle. *Review of Earth and Planetary Sciences*, *34*(1), 629–653. https://doi.org/10.1146/annurev.earth.34.031405.125211

Inoue, T., Wada, T., Sasaki, R., & Yurimoto, H. (2010). Water partitioning in the Earth's mantle. *Physics of the Earth and Planetary Interiors*, *183*(1-2), 245–251. https://doi.org/10.1016/j.pepi.2010.08.003

Ishii, M., & Tromp, J. (1999). Normal-mode and free-air gravity constraints on lateral variations in velocity and density of Earth's mantle. *Science*, *285*(5431), 1231–1236. https://doi.org/10.1126/science.285.5431.1231

Karki, B. B., & Stixrude, L. (2010). First-principles study of enhancement of transport properties of silica melt by water. *Physical Review Letters*, *104*(21), 215901. https://doi.org/10.1103/PhysRevLett.104.215901

Karki, D., Ghosh, B., Maharjan, C. M., Karato, S.-I., & Park, J. (2018). Density-pressure profiles of Fe-bearing $MgSiO_3$ liquid: Effects of valence and spin states, and implications for the chemical evolution of the lower mantle. *Geophysical Research Letters*, *45*, 3959–3966. https://doi.org/10.1029/2018GL077149

Kono, Y., & Sanloup, C. (2018). *Magma under pressure*, (p. 497). Amsterdm: Elsevier.

Korenaga, J. (2008). Urey ratio and the structure and evolution of Earth's mantle. *Reviews of Geophysics*, *46*, RG2007. https://doi.org/10.1029/2007rg000241

Kresse, G., & Furthmüller, J. (1996). Efficiency of ab-initio total energy calculations for metals and semiconductors using a plane-wave basis set. *Computational Materials Science*, *6*(1), 15–50. https://doi.org/10.1016/0927-0256(96)00008-0

Kurz, M. D., Jenkins, W. J., & Hart, S. R. (1982). Helium isotopic systematics of oceanic islands and mantle heterogeneity. *Nature*, *297*(5861), 43–47. https://doi.org/10.1038/297043a0

Labrosse, S., Hernlund, J. W., & Coltice, N. (2007). A crystallizing dense magma ocean at the base of the Earth's mantle. *Nature*, *450*(7171), 866–869. https://doi.org/10.1038/nature06355

Lau, H. C. P., Mitrovica, J. X., Davis, J. L., Tromp, J., Yang, H. Y., & Al-Attar, D. (2017). Tidal tomography constrains Earth's deep-mantle buoyancy. *Nature*, *551*(7680), 321–326. https://doi.org/10.1038/nature24452

Litasov, K., Ohtani, E., Langenhorst, F., Yurimoto, H., Kubo, T., & Kondo, T. (2003). Water solubility in Mg-perovskites, and water storage capacity in the lower mantle. *Earth and Planetary Science Letters*, *211*(1-2), 189–203. https://doi.org/10.1016/S0012-821X(03)00200-0

Matsukage, K. N., Jing, Z., & Karato, S.-I. (2005). Density of hydrous silicate melt at the conditions of Earth's deep upper mantle. *Nature*, *438*(7067), 488–491. https://doi.org/10.1038/nature04241

Meade, C., Reffner, J. A., & Ito, E. (1994). Synchrotron infrared absorbency measurements of hydrogen in $MgSiO_3$ perovskite. *Science*, *264*(5165), 1558–1560. https://doi.org/10.1126/science.264.5165.1558

Mibe, K., Kanzaki, M., Kawamoto, T., Matsukage, K. N., Fei, Y. W., & Ono, S. (2007). Second critical endpoint in the peridotite-H_2O system. *Journal of Geophysical Research*, *112*, B03201. https://doi.org/10.1029/2005jb004125

Miyazaki, Y., & Korenaga, J. (2019). On the timescale of magma ocean solidification and its chemical consequences: 2. Compositional differentiation under crystal accumulation and matrix compaction. *Journal of Geophysical Research: Solid Earth*, *124*, 3399–3419. https://doi.org/10.1029/2018jb016928

Mookherjee, M., Stixrude, L., & Karki, B. (2008). Hydrous silicate melt at high pressure. *Nature*, *452*(7190), 983–986. https://doi.org/10.1038/nature06918

Mosenfelder, P., Asimow, D., & Ahrens, T. J. (2007). Thermodynamic properties of Mg_2SiO_4 liquid at ultra-high pressures from shock measurements to 200 GPa on forsterite and wadsleyite. *Journal of Geophysical Research*, *112*, B06208. https://doi.org/10.1029/2006JB004364

Mosenfelder, P., Asimow, D., Frost, D. J., Rubie, D. C., & Ahrens, T. J. (2009). The $MgSiO_3$ system at high pressure: Thermodynamic properties of perovskite, postperovskite, and melt from global inversion of shock and static compression data. *Journal of Geophysical Research*, *114*, B01203. https://doi.org/10.1029/2008JB005900

Murakami, M., Hirose, K., Yurimoto, H., Nakashima, S., & Takafuji, N. (2002). Water in Earth's lower mantle. *Science*, *295*(5561), 1885–1887. https://doi.org/10.1126/science.1065998

Nomura, R., Hirose, K., Uesugi, K., Ohishi, Y., Tsuchiyama, A., Miyake, A., & Ueno, Y. (2014). Low core-mantle boundary temperature inferred from the solidus of pyrolite. *Science*, *343*(6170), 522–525. https://doi.org/10.1126/science.1248186

Nomura, R., Ozawa, H., Tateno, S., Hirose, K., Hernlund, J., Muto, S., et al. (2011). Spin crossover and iron-rich silicate melt in the Earth's deep mantle. *Nature*, *473*(7346), 199–202. https://doi.org/10.1038/nature09940

Ohnishi, S., Kuwayama, Y., & Inoue, T. (2017). Melting relations in the MgO–$MgSiO_3$ system up to 70 GPa. *Physics and Chemistry of Minerals*, *44*(6), 445–453. https://doi.org/10.1007/s00269-017-0871-8

Panero, W. R., Pigott, J. S., Reaman, D. M., Kabbes, J. E., & Liu, Z. (2015). Dry (Mg,Fe)SiO_3 perovskite in the Earth's lower mantle. *Journal of Geophysical Research: Solid Earth*, *120*, 894–908. https://doi.org/10.1002/2014JB011397

Petitgirard, S., Malfait, W. J., Sinmyo, R., Kupenko, I., Hennet, L., Harries, D., et al. (2015). Fate of $MgSiO_3$ melts at core-mantle boundary conditions. *Proc Natl Acad Sci U S A*, *112*(46), 14,186–14,190. https://doi.org/10.1073/pnas.1512386112

Solomatov, V. S., & Stevenson, D. J. (1993a). Suspension in convective layers and style of differentiation of a terrestrial magma ocean. *Journal of Geophysical Research - Planets*, *98*(E3), 5375–5390. https://doi.org/10.1029/92je02948

Solomatov, V. S., & Stevenson, D. J. (1993b). Nonfractional crystallization of a terrestrial magma ocean. *Journal of Geophysical Research - Planets*, *98*(E3), 5391–5406. https://doi.org/10.1029/92je02579

Solomatova, N. V., Caracas, R., & Manning, C. E. (2019). Carbon sequestration during core formation implied by complex carbon polymerization. *Nature Communications*, *10*(1), 789. https://doi.org/10.1038/s41467-019-08742-9

Stevenson, D. J. (2008). A planetary perspective on the deep Earth. *Nature*, *451*(7176), 261–265. https://doi.org/10.1038/nature06582

Tateno, S., Hirose, K., & Ohishi, Y. (2014). Melting experiments on peridotite to lowermost mantle conditions. *Journal of Geophysical Research: Solid Earth*, *119*, 4684–4694. https://doi.org/10.1002/2013JB010616

Thomas, C. W., Liu, Q., Agee, C. B., Asimow, P. D., & Lange, R. A. (2012). Multi-technique equation of state for Fe_2SiO_4 melt and the density of Fe-bearing silicate melts from 0 to 161 GPa. *Journal of Geophysical Research*, *117*, B10206. https://doi.org/10.1029/2012JB009403

Tonks, W. B., & Melosh, H. J. (1993). Magma ocean formation due to giant impacts. *Journal of Geophysical Research - Planets*, *98*(E3), 5319–5333. https://doi.org/10.1029/92JE02726

Trampert, J., Deschamps, F., Resovsky, J., & Yuen, D. (2004). Probabilistic tomography maps chemical heterogeneities throughout the lower mantle. *Science*, *306*(5697), 853–856. https://doi.org/10.1126/science.1101996

Williams, Q., & Garnero, E. J. (1996). Seismic evidence for partial melt at the base of Earth's mantle. *Science*, *273*(5281), 1528–1530. https://doi.org/10.1126/science.273.5281.1528

Yuan, K., & Romanowicz, B. (2017). Seismic evidence for partial melting at the root of major hot spot plumes. *Science*, *357*(6349), 393–397. https://doi.org/10.1126/science.aan0760

Erratum

In the originally published version of this article, there were errors published in the Abstract. These errors have since been corrected, and the present version may be considered the authoritative version of record.